

The multichannel triple-laser interferometer/polarimeter system at RTP^{a)}

J. H. Rommers, A. J. H. Donné, and F. A. Karelse

FOM—Instituut voor Plasmafysica 'Rijnhuizen,' Association Euratom-FOM, P.O. Box 1207,
3430 BE Nieuwegein, The Netherlands

J. Howard

Plasma Research Laboratory, Australian National University, Canberra, A.C.T. 0200, Australia

(Received 13 May 1996; accepted for publication 13 June 1996)

A 19-channel combined interferometer and polarimeter system has recently become operational at the Rijnhuizen Tokamak Project ($a=0.164$ m, $R=0.72$ m, $B_{\text{tor}}\leq 2.5$ T, $I_p\leq 150$ kA, plasma pulse duration ≤ 500 ms), in order to determine the poloidal magnetic field and plasma density distribution simultaneously. The method is based on the separate propagation of two counter-rotating, circularly polarized probing waves, and enables high temporal resolution measurements of both the interferometric and the polarimetric phase change using only one detector per line of sight. In this article a thorough discussion of the (polarization-related) optical, electronic, and computational aspects of the system will be presented. © 1997 American Institute of Physics. [S0034-6748(97)00402-4]

I. INTRODUCTION

Various methods for performing combined interferometry and polarimetry on magnetically confined plasmas have been developed. The most recent generation of interferometer/polarimeter systems is based on a modulation or a continuous rotation of the polarization vector. The principle advantage of these systems lies in the fact that a single detection element is used for measuring the density-induced phase shift as well as the rotation of the polarization plane due to the Faraday effect. A drawback is that the polarization modulation in most of these systems is achieved mechanically, which imposes constraints on the maximum achievable temporal resolution. Moreover, many of these methods suffer from crosstalk between the polarimeter and interferometer signal.

To overcome the typical drawbacks of the present generation of polarization modulated systems, a new method for performing combined interferometry and polarimetry on magnetically confined plasmas has been developed and applied to the Rijnhuizen Tokamak Project (RTP). The method employs three separate far-infrared laser beams to probe the refractive indices of the polarization eigenmodes in the plasma. Since no mechanical polarization modulation techniques are used, the achievable temporal resolution is, in principle, limited by signal-to-noise considerations and can be as high as several tens of kHz.

The new scheme for combined interferometry/polarimetry has recently been presented in literature,¹ with the emphasis on a thorough description of the measurement principle. In the underlying article a detailed presentation of the instrumentation is given. In Sec. II a brief recapitulation of the measurement principle is given, followed by a discussion of the optical layout of the system implemented at the RTP tokamak. In Sec. III we address some of the difficulties associated with the generation and propagation of circularly

polarized beams. Here the emphasis will be on the application of quartz quarter wave plates for the creation of circularly polarized waves, and the application of electroformed nickel meshes for beam splitting purposes. Section IV of the article is focused on the electronic setup, which for the RTP system has been kept simple and flexible. The carrier signals are subsampled (and hence aliased into a lower frequency band) and signal demodulation is performed in software. Some of the advantages of this approach are illustrated. These include, for example, the possibility to compute the signal amplitude as a function of time, which can be valuable in situations of high refraction. The effect of severe refraction on Abel inversion for the RTP system is discussed in Sec. V, followed by a presentation of a typical result. The RTP tokamak is characterized by $a=0.164$ m, $R=0.72$ m, $B_{\text{tor}}\leq 2.5$ T, $I_p\leq 150$ kA, and plasma pulse duration ≤ 500 ms. The rest of the diagnostic park is described by Donné *et al.*²

II. THE INTERFEROMETER/POLARIMETER SYSTEM

A. Principle

The new interferometer/polarimeter scheme utilizes two distinct but colinear beams to probe the plasma (see Fig. 1), and a third one to serve as a local oscillator (LO). The two probing beams are slightly frequency offset and their polarizations are set to counter-rotating circular. Because of birefringence, the beams will experience a different value of the refractive index during propagation through the plasma. This difference in refractive index is related to the Faraday rotation angle, whereas their average is related to the density induced phase shift.³

Upon emerging from the plasma, the probing beams pass through a polarizer that transmits the polarization component in the toroidal direction. The two beams, which were initially orthogonal, are now free to interfere and are combined with the linearly polarized local oscillator (LO) beam (also slightly frequency offset from the probe beams) to give a

^{a)}The abstract for this article was published in Rev. Sci. Instrum. **68**, 446 (1997).

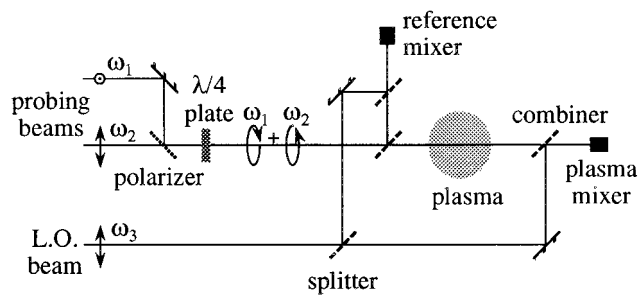


FIG. 1. Schematic depiction of the polarimeter setup at RTP. Two laser beams with angular frequencies ω_1 and ω_2 are transmitted through the plasma in orthogonal circular polarization states. Coalignment of the two beams is achieved without power loss using a polarizer/quarter wave plate combination. A third laser at frequency ω_3 acts as local oscillator for heterodyne detection of the interferometric phase shift.

total of three primary intermediate frequency signals (or mixing products) at the detector.

The frequency offsets that allow us to distinguish and separately demodulate the independent carriers can be generated either by using a Doppler wheel or with a multiple laser system with slightly detuned cavities. The individual phases of each of the mixing products can then be determined and compared with those from a reference interferometer. The recovered phase shifts are those suffered separately by the two probing beams, obtained via mixing with the LO, as well as their phase difference, obtained via their mutual mixing product. The latter phase difference is directly proportional to the Faraday rotation angle, but this quantity can also be obtained indirectly by taking the difference between the phases of the probe-LO mixing products. The interferometer phase shift is obtained by taking the average of the two probe-LO phases. The time resolution of the measurement is theoretically set by the frequency separation between the mixing products and can easily be of the order of several hundred kHz. However, in practice signal-to-noise considerations limit the maximum achievable time resolution to several tens of kHz.

B. Layout

In the RTP combined interferometer and polarimeter system (see Fig. 2), a single high-power (≥ 150 W) CO₂ laser is used to pump three separate far-infrared (FIR) laser cavities. Two of these are used to generate the probing beams while the third laser provides the local oscillator power. The CO₂ laser wavelength of $9.27 \mu\text{m}$ is suitable for pumping the $432.5 \mu\text{m}$ line of formic acid, the lasing medium. Each FIR laser cavity produces linearly polarized sub-millimeter radiation at a power level of approximately 30 mW.

The two probing beams are coaligned directly behind the laser. A half wave plate is used to rotate the polarization of one of the beams and the resulting orthogonal linear polarizations are coaligned without power loss using a polarizer to reflect one of the beams and to transmit the other.

The probing beams are transported towards the tokamak experiment by means of a single, highly oversized (70 mm

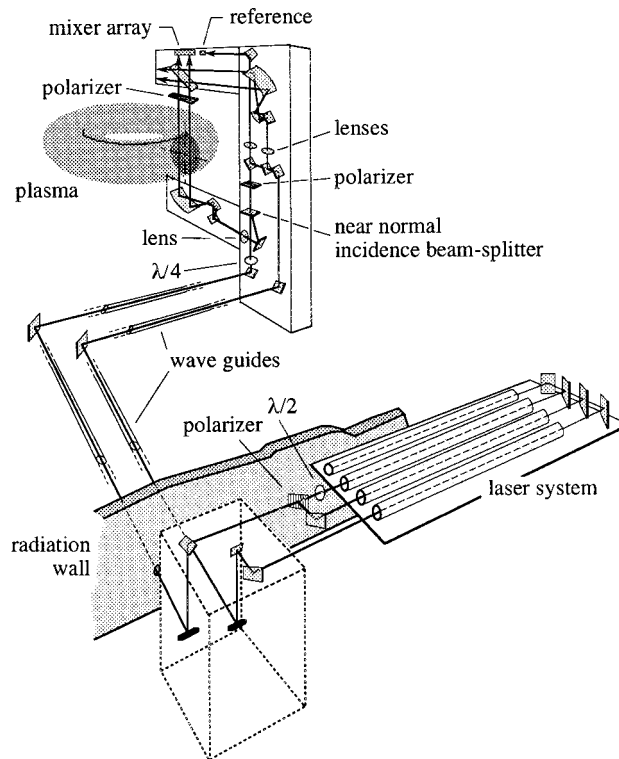


FIG. 2. Combined interferometer/polarimeter setup at RTP.

inner diameter) circular waveguide with a length of approximately 7 m. A second waveguide is used for transporting the LO beam to the detector array. In all cases, the beams are focused onto the entrance plane of the waveguide with a waist diameter of approximately 20 mm at the $1/e$ level of the beam intensity for efficient coupling of the beam into the waveguide.^{4,5}

Near the tokamak, the two probing beams are passed through a single quarter wave plate to convert the polarizations to counterrotating circular. A beam splitter is then used to sample some power for the reference interferometer. Most of the power ($\approx 95\%$) is reflected at a small angle to the incident beam and sent through a one-dimensional parabolic mirror system. This mirror system creates a slablike beam that is enlarged in the radial direction by a factor of 7.5. A one-dimensional lens acting in the toroidal direction produces a beam waist close to the plasma center. Upon emerging from the vessel, the probing beams traverse the wire grid polarizer and are combined with the LO. Apart from the absence of a wave plate and polarizer, the LO beam follows an optical path equivalent to that of the probing beams.

The interference of the three independent beams is sensed using an array of up to 19 Schottky diode corner cube mixers. These devices can operate up to extremely high frequencies and have excellent S/N characteristics,⁶ even at room temperature. For the RTP setup, postdetection electronics low-pass bandlimit the signals to several MHz and provide 60 dB amplification for each signal. The laser power is coupled onto the detector whisker and diode using fixed parabolic mirrors attached to each corner cube. The whisker coupling makes the detectors extremely polarization selec-

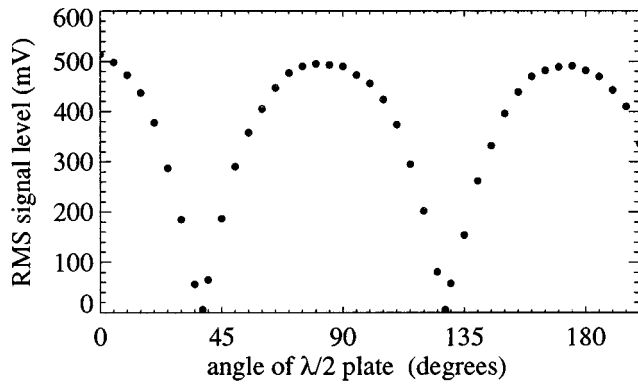


FIG. 3. Mixer polarization sensitivity, measured by rotating the polarization of the ‘‘probing beam.’’ At 38° , a signal level of 5.6 mV was obtained, corresponding to 1.1% of the maximum.

tive, as demonstrated by Fig. 3. The parabolic mirror is designed to collect all the available signal power in toroidal direction, while its radial width of 14 mm fixes the transverse spatial resolution of the line-integrated measurement.

The detection electronics, including the mixers, is mounted in a shielded cage to minimize electromagnetic pick-up. The laser radiation enters the cage through a Fabry–Pérot filter constructed of two sheets of nickel mesh. The mesh period is chosen such that the finesse (the ratio of peak width at half-maximum to distance between two consecutive maxima) of the Fabry–Pérot is low at the laser wavelength while high at either of the wavelengths of the microwave heating sources at RTP (2.7 and 5.0 mm). This is possible because the mesh period normalized to the wavelength of the incident light determines the reflectivity of a single sheet, and because the reflectivity of the individual sheets determines the finesse.

C. Gaussian beam propagation

The laser beam propagation after the waveguide exit has been determined from beam profile measurements, and is shown in Fig. 4. From the fitted beam parameters, a Gaussian beam tracing code has been used to model the free-space propagation of the laser beams through the system (see Fig. 5). Because of the beam asymmetries in the plasma arm of the interferometer, separate calculations have been performed for the radial and toroidal directions. The parabolic mirror system ($f=4$ and 30 cm) expands the beams radially, while the one-dimensional lenses focus toroidally. A minor further improvement in probing beam focus could be obtained by shifting the position of the lens, but this is in practice difficult because of space limitations.

For diffraction-free propagation of a beam through an optical system, one requires that the beam be truncated at a power level no greater than 1% of the peak.⁵ In the case of a Gaussian beam, this is equivalent to the requirement that all optics should at least be 2.2 times as wide as the local $1/e$ beam diameter. In the RTP system, most optical elements have a size of at least 80 mm, which is just sufficient for unperturbed propagation of the beams through the optical system. The major exceptions to this are the given access

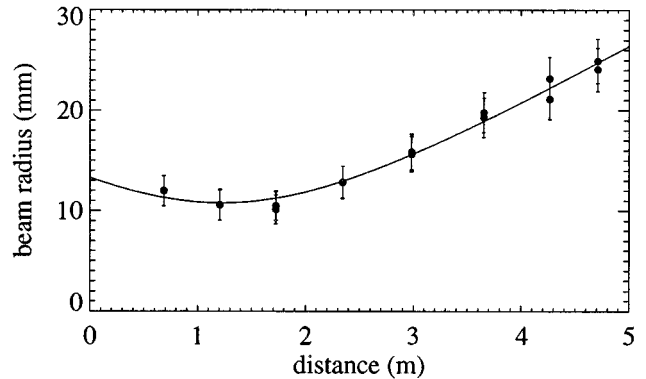


FIG. 4. Measured beam propagation for a probing beam as a function of distance after the waveguide exit, without any further optics. A waist diameter of 21 mm has been established at 1.2 m behind the waveguide exit.

ports of the tokamak vessel (see Fig. 6) which have a maximum width of 45 mm in the toroidal direction, tapering down to 24 mm on the high-field side of the torus. Minor distortions of the phase front are therefore likely, in particular at the high-field side. Moreover, the width of the profile along the major radius is such that truncation and hence diffraction is as well to be expected in that direction.

III. POLARIZATION CONSIDERATIONS

A. Generating circularly polarized beams

The polarimetric method at RTP relies on the propagation of circularly polarized waves through the plasma. Any distortion of the wave polarization may lead to errors in the measurement.¹ The polarizations of both probing waves are set to linear by the low-leakage combining polarizer. After transport to the machine hall, the beams are converted to circular by a single quarter wave plate, mounted at the waveguide exit. In the process of creating these circularly polarized waves, distortions can be introduced either because of wave plate errors or because of inaccuracies in the wave polarization incident on the wave plate. A measurement of the linearity and orthogonality of the wave polarizations emerging from the waveguide is given in Fig. 7 and does not indicate any significant distortion.

The action of a quarter wave plate relies on a difference in the refractive index along the two orthogonal optical axes of the plate. The thickness of a quarter (half) wave plate is chosen such that the associated difference in phase velocity leads to a phase retardation along the slow axis of 90° (180°) relative to the fast axis. In the far infrared, wave plates are often made of crystal quartz because of its negligible absorption loss. Plate thicknesses at $432.5 \mu\text{m}$ are 2.3 and 4.6 mm, respectively, for a single-order quarter and half wave plate.

In order to avoid beam deflection by the wave plate, the plate surfaces must be parallel to high accuracy. However, this requirement also leads to the occurrence of standing waves inside the material, as demonstrated by the measurement of Fig. 8. While the incident linearly polarized wave was aligned with either the fast or the slow axis of the plate,

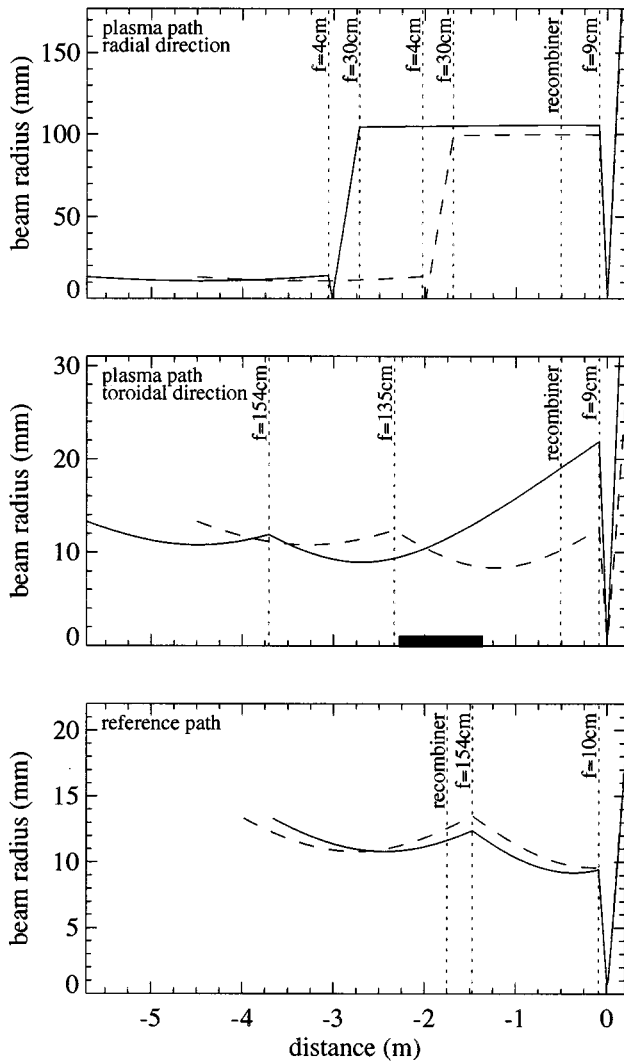


FIG. 5. Calculated Gaussian propagation of both the probing beams (solid lines) and the LO beam (dashed) through the system, based upon the measured behavior at the waveguide exit (Fig. 4). The plasma branch behaves differently in radial direction (top plot) than in toroidal direction (middle) because of the one-dimensional curvature of some of the lenses and parabolic mirrors. In the reference branch only two-dimensional optics is used. The x axis is chosen so that the mixer position is at zero. Because of differences in optical path lengths, the waveguide exit positions (starting point of each trace) are not identical. For the probing beam, the black bar indicates the vessel position.

its apparent thickness was increased by tilting the plate about this axis. After converting the tilt angle to an equivalent change in the optical path length the presence of standing waves is evident. Positive interference results in total trans-

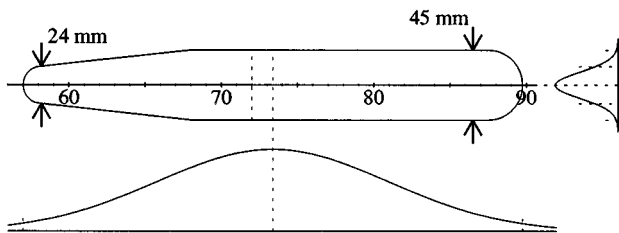


FIG. 6. Size and shape of the RTP port, and a comparison with the widths of the calculated Gaussian beam profiles from Fig. 5 at the exit port.

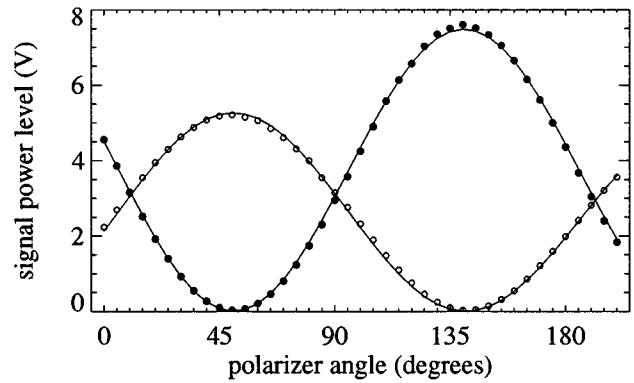


FIG. 7. Measured polarization purity and orthogonality of both linearly polarized probing beams at the waveguide exit. A pyro-electric detector has been used to measure the power in each of the beams, and a rotatable polarizer is used to filter the emerging beam polarization. From the solid cosines fitted to the data, the angle between the polarization directions was determined to be $90.6^\circ \pm 0.2^\circ$.

mission at normal incidence along both axes of the half wave plate. Since the double-pass phase lag between fast and slow wave is only 180° inside the quarter wave plate, positive interference along one of the axes necessarily involves destructive interference along the other, and one component is partially reflected. The resulting difference in transmissivity between the two optical axes implies that waves incident with linear and orthogonal polarizations cannot simultaneously be converted into counter-rotating circularly polarized waves.

To eliminate the standing wave effect, an impedance matching polyethylene coating was applied to both sides of the wave plate. In Fig. 9 the result of a measurement of the polarization component of the transmitted wave both parallel and perpendicular to the incident linearly polarized wave is

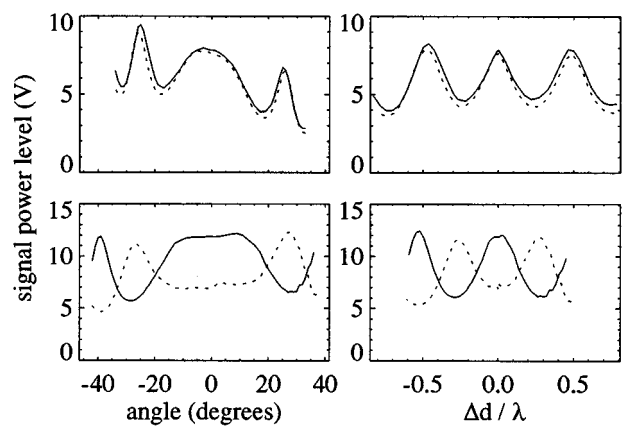


FIG. 8. Measurement of the transmitted power through an uncoated quartz half (top plots) and quarter wave plate (bottom plots), using a beam with its linear polarization aligned along one of the optical axes of the wave plate (solid/dashed lines). The left plots show the raw data, while for the right, the angle of incidence has been converted to an increase of optical path length inside the plate (the sign is artificial). A first-order correction has been applied to correct for the power decrease caused by the displacement of the beam across the detector surface.

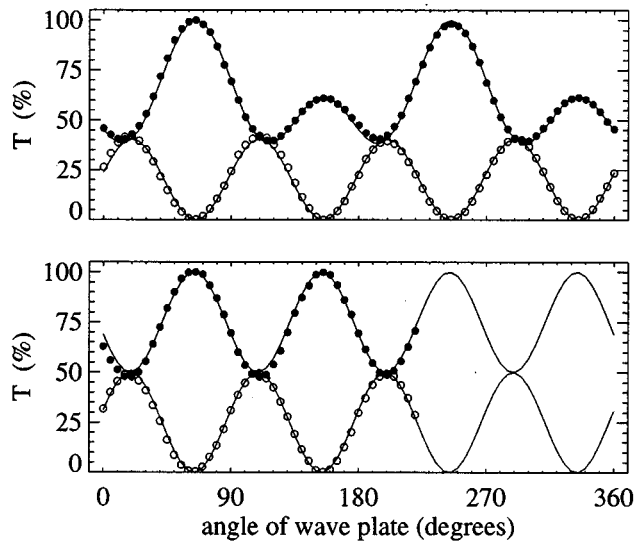


FIG. 9. Measurement of the quarter wave plate behavior before and after coating. The power has been measured for the transmitted component with polarization parallel to the incident polarization (solid dots) as well as for the orthogonal component (open dots), both before (top) and after coating (bottom). Model calculations are also plotted (solid line), where for the uncoated case transmissivities along the axes of 100% and 62% have been assumed. For the coated case both were assumed to be 100%.

shown for a quarter wave plate before and after coating. Here the wave plate is rotated around its geometrical axis in order to vary the ellipticity of the transmitted wave. A comparison with theoretically obtained curves is made, where a power transmissivity of 62% is assumed along the reflecting axis of the uncoated plate. From literature values for the refractive index (2.116 and 2.163 for fast and slow wave, respectively⁷) one can calculate^{8,9} a single-surface reflectivity of 13% at normal incidence and a minimum Fabry–Pérot transmissivity of 59%, which is in good agreement with the experimental value of 62%.

B. Polarization conservation

Both metallic and dielectric reflectors generally exhibit different reflectivities for p - and s -mode reflections, i.e., reflections where the polarization is either in or perpendicular to the plane of incidence. Therefore those optical elements form a potential hazard from the point of view of polarization conservation. Reflections from metallic surfaces can be characterized by a complex refractive index $N + jK$, where K is the extinction coefficient of the wave in the metal. In the submillimeter region the values for both N and K are extremely large, and the reflectivity of a metallic surface is for both p - and s -mode always very close to 100%. Moreover, except for angles of incidence greater than 85° , there is no differential phase change upon reflection. In the far infrared, we can thus effectively ignore any polarization distortions attending the use of metallic mirrors.

In the RTP setup, sheets of electroformed Nickel mesh are used as partial reflectors. The wire spacings g and widths a of these meshes are optimized for a certain reflectivity. A list of typical mesh types and parameters is given in Table I. The transmissivity for three mesh types was measured as a

TABLE I. Manufacturer specified parameters of the meshes used in the polarimeter setup and in the transmission measurements. The wire width is indicated by a , the grid period by g . For calculation of the derived parameter g/λ , λ is taken to be $432.5 \mu\text{m}$. Mesh thickness is approximately $3.8 \mu\text{m}$.

Mesh type (lpi)	$g(\mu\text{m})$	$a(\mu\text{m})$	g/a	g/λ
100	254.00	35.56	7.143	0.5873
150	169.41	30.74	5.511	0.3917
400	64.01	14.74	4.343	0.1480
500	51.05	11.68	4.371	0.1180

function of the angle of incidence (power absorption by the mesh is negligible). Results for both p -mode and s -mode transmission are given in Fig. 10. Note the pronounced bifurcation in the behavior of the 100 lpi mesh at incidence angles near 45° .

Marcuvitz¹⁰ has developed a model for describing the behavior of a one-dimensional wire grid using equivalent electrical circuits. In the model, a dependence on the angle of incidence has been included, provided that the wires are directed perpendicular to the plane of incidence. When the incident E -vector is perpendicular to the wires, and hence in the plane of incidence, reflection is mainly due to capacitive coupling between the grid and the wave. The amount of coupling is a function of a/g , and is negligible for the mesh types under consideration, for which a/g is of order 0.2. When the E -vector is parallel to the wires (and hence perpendicular to the plane of incidence) the coupling is mainly inductive and the model predicts an appreciable reflection

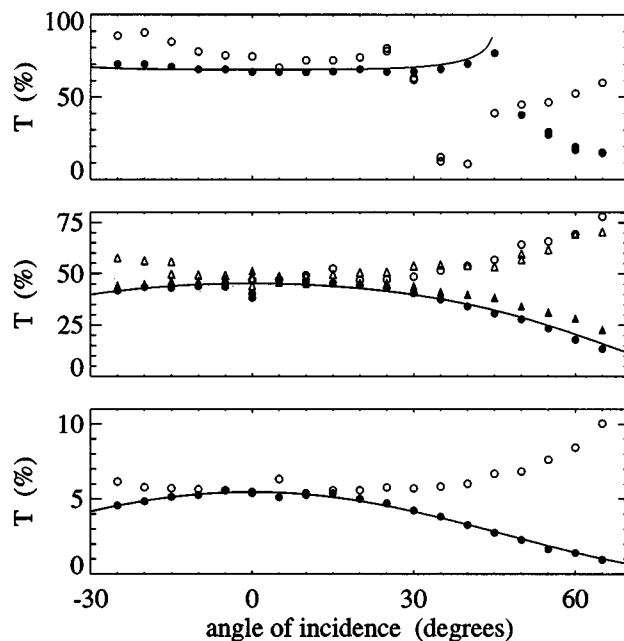


FIG. 10. Measured and calculated power transmissivities for a 100, a 150 and a 400 lpi mesh, respectively, as a function of the angle of incidence. The mesh structure was aligned parallel to the plane of incidence (circles) or at an angle of 45° (triangles). The solid symbols indicate s -mode and the open symbols p -mode reflection. Values of the wire width a used in the theoretical fit are 58.6, 36.8, and $18.8 \mu\text{m}$, respectively.

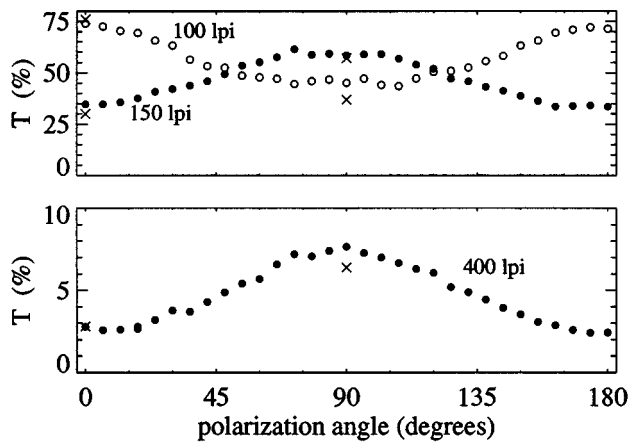


FIG. 11. Measured power transmissivity of the 100 and 150 lpi mesh (left plot) as well as the 400 lpi mesh (right plot), all as a function of the angle that the incident polarization makes with the plane of incidence of the mesh. The angle of incidence is 45° and the mesh structure is aligned parallel to the plane of incidence. The crosses indicate the equivalent datapoints from the measurement of Fig. 10.

coefficient. The model does not take into account any higher-order diffraction modes, which are to be expected in case $g(1 + \sin \theta_i) > \lambda$. In the case of the 100 lpi mesh, the observed behavior near 45° coincides with the transition from single-order to multiple-order transmission. In the case of p -mode reflection, inductive coupling to the grid wires lying in the plane of incidence is the dominant reflection mechanism, and the theory does not apply.

Marcuvitz's model can be used to describe the behavior of the s -mode reflection, as measured and plotted in Fig. 10, because inductive reflection from the wires perpendicular to the plane of incidence dominates the capacitive reflection from the wires in that plane. The results of the model calculations are plotted in Fig. 10 as solid lines. In order to improve the agreement with the measurements, the values of the wire width have been increased by 20%–60% over those of Table I. Direct measurement of the wire width a on various samples of similar mesh showed a large spread from sample to sample, but a tendency towards higher values than specified by the manufacturer. Given the crudeness of the model, which neglects the two-dimensionality of the grid altogether and assumes zero mesh thickness as well as a well-defined constant wire width, the agreement between model and experiment is acceptable. The model accounts well for the behavior of the 100 lpi mesh up to an incident angle of 45° .

One may also study the transmission of the meshes at a constant angle of incidence, while the orientation angle of the incident linear polarization is varied from s - to p -type. Measurements are presented in Fig. 11, for an incident angle of 45° . Again the behavior of the 100 lpi mesh is quite different from the others, because the incidence angle is close to the diffraction transition. A quantitative comparison with the previous type of measurement indicates good agreement.

It is experimentally verified then, that nickel mesh partial beam reflectors can exhibit large differences between

p - and s -mode transmissivities (and hence reflectivities) for non-normal incidence. In the RTP setup, it is necessary to use partial reflectors twice for beam splitting and twice for combining. However, in three cases the beams involved are linearly polarized along the s -axis and therefore no distortion is introduced. Only the mesh that allows some leakage of the probing beam power for the reference interferometer is likely to cause problems. The measurements from Fig. 10 indicate only a weak dependency of the transmissivity on the angle of incidence, provided that the angle of incidence does not exceed 15° . Thus, mounting the beam splitter (constructed in this case from a 400 lpi mesh) at near-normal incidence, as shown in Fig. 2, ensures that there is no significant distortion of the polarization state.

IV. SIGNAL PROCESSING

A. Data acquisition

The three independent FIR laser cavities are tuned so that the mixer signals contain three appropriately frequency-separated phase-modulated carrier waves. Before digitization, the signals are preamplified (60 dB low noise) and conditioned using variable amplifiers/attenuators and bandpass filters (passband of 0.1–5 MHz) to match the input voltage range of the analog to digital converters (ADCs). The pass-band is compatible with the range of beat or intermediate frequencies (IFs) generated through mixing under normal operating conditions.

The maximum ADC sampling frequency is 1 MHz. However, only at 500 kHz the on-board memory is sufficiently large to acquire the whole duration of a standard-length plasma discharge (0.5 s). For stability reasons the laser system has to be operated with IFs that are well above the associated Nyquist frequency. The signals are nevertheless fed directly into the ADCs, and the carriers are folded into the accessible frequency band as a result of aliasing.¹¹ If care is taken that none of the IFs is close to (an integer multiple of) the Nyquist frequency, and if, moreover, aliasing does not cause the different frequency peaks to overlap, the measurement is not significantly affected.

The RTP laser system can be operated in two different modes compatible with this controlled aliasing, shown schematically in Fig. 12. In both modes, two of the IFs are set in the interval between two and three times the Nyquist frequency. The third frequency is then also determined except for a sign freedom: $df_3 = |df_1 \pm df_2|$, where df_i indicates the i th mixing frequency. In the case of a minus sign, two of the actual laser frequencies are very close, and df_3 is suppressed by the electronics. If there exists some coupling between the close lasers due to radiation feedback (this is difficult to completely eliminate), frequency pulling may occur and affect the frequency stability of both. Therefore the operating mode associated with the plus sign is usually preferred. In that case all three laser peaks are transmitted by the bandpass filters and the Faraday rotation angle can be determined both directly from the phase of the mixing product between the two probes, and from the difference between the phases of the two probe–LO mixes. One can optimize the measurement by constructing a S/N weighted average of the two. In

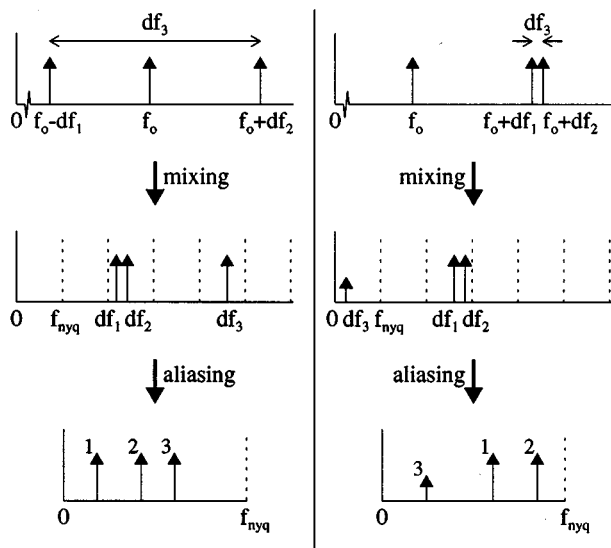


FIG. 12. Possible laser operating modes compatible with both the electronic hardware and the ADC Nyquist frequency. The top figure shows the laser frequencies, the middle one the beat frequencies obtained after mixing, and the bottom the spectrum obtained after aliasing (the frequency axis has been enlarged four times). An arbitrary reference laser frequency is indicated with f_0 , whereas df_1 , df_2 , and df_3 are the three beat frequencies obtained after mixing. In the rightmost operating mode, df_3 is rather low and hence suppressed by the electronics.

practice, the probe–probe mixing peak may, in particular for the channels at the high-field side of the tokamak, give a somewhat lower S/N level, because of loss of beam power due to the tapering of the window (see Fig. 6), which does not affect the LO beam.

As a consequence of the controlled aliasing, the available frequency bandwidth is limited by the Nyquist frequency. In the ideal case, where the three laser lines are evenly distributed over the available band, each peak has a double-sided bandwidth of one-third of the Nyquist frequency. This limits the temporal resolution in the determination of the phase of each peak to one sixth of the Nyquist frequency, which is 40 kHz. Obviously, this ideal situation can in practice not be reached, both because the three IFs are not all independent, which makes an even distribution impossible, and because the accuracy with which the lasers can be set is limited by the frequency stability, which is in the range of 5–10 kHz. Therefore, great care has been taken to eliminate causes for frequency drifting, in particular mechanical vibrations and temperature variations.

B. Phase demodulation

A complex signal analysis algorithm (schematically depicted in Fig. 13) has been developed to computationally derive the evolution of the individual peak phases from the acquired signal. After the data has been windowed and Fourier transformed, the central frequency of each beat signal is determined. Each of the IFs are isolated in turn using band-

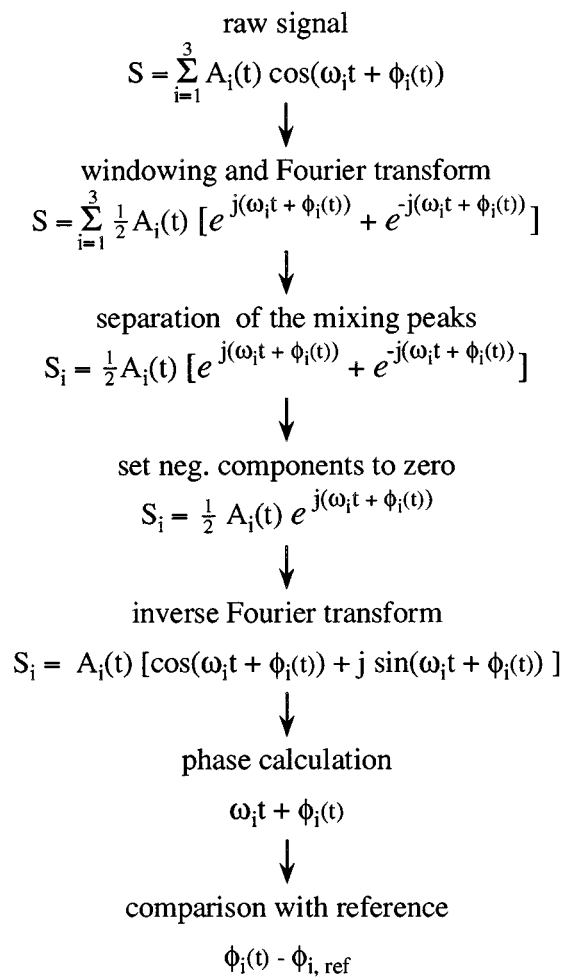


FIG. 13. Analysis algorithm (see the text).

pass filters centered on the carrier frequency. An example of an initial spectrum and its associated filters is given in Fig. 14. The broadness of the peaks is mainly due to instability in the carrier frequency. Additional (polluting) peaks result

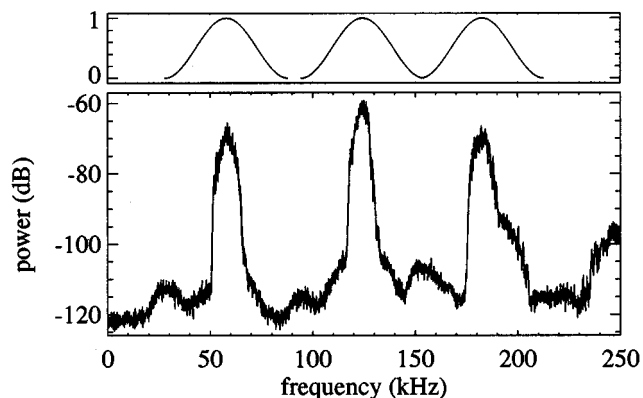


FIG. 14. Reference spectrum for an Ohmic discharge, constructed from a digitized interferogram of duration 525 ms (covering the period of the discharge). The original spectral resolution of 1.9 Hz has been reduced to 61 Hz by averaging. The peak at 124 kHz corresponds to mixing between the probes, whereas those at 58 and 182 kHz are due to mixing between probe 1 and 2 with the LO, respectively. A disturbance peak that slightly interferes with the 182 kHz signal peak is too low to cause significant distortion. For peak separation, three cosine bandpass filters with an overall width of 60 kHz are used (top plot).

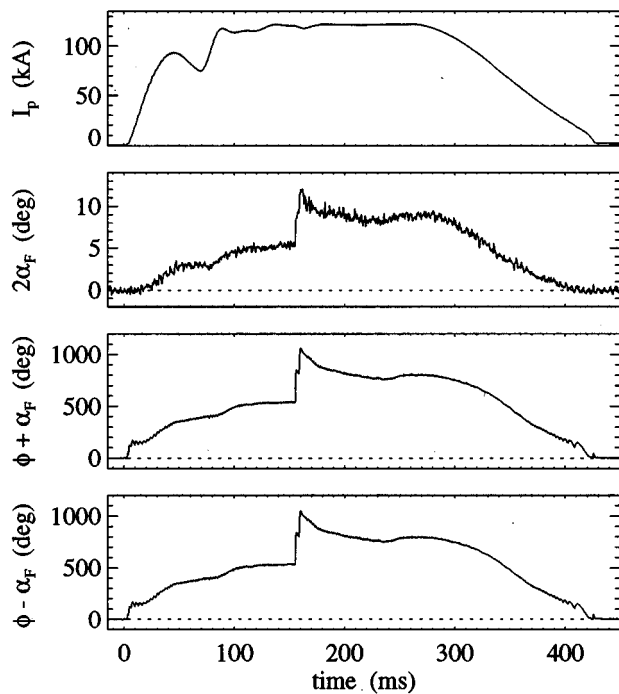


FIG. 15. Ohmic discharge in which two relatively small pellets (4.8×10^{18} and 3.5×10^{18} atoms) are injected at 155 and 159 ms. The discharge current is plotted, as well as the phases of each of the three mixing peaks after analysis, for a high-field side detector at $r/a = -0.49$. The second plot yields the phase of the probe-probe mix, which is equal to twice the Faraday rotation angle. The third and fourth plot yield the phases of both probe-LO mixes. The associated spectrum is given in Fig. 14. After phase calculation, a 2 kHz low-pass filter has been used to eliminate high-frequency noise.

from aliased harmonics generated because of diode nonlinearity. However, the levels of these harmonics are too low to significantly distort the measurement, and, moreover, they are often suppressed in the separation process. Both for windowing and filtering, cosine tapers are used to minimize any edge effects.

For each of the isolated spectra, the negative frequency components are set to zero, as part of a mathematical procedure to calculate the signal phase.¹² As a consequence the signal phase is obtained from the associated time domain analytic signals by calculating the arctangent of the quotient of the imaginary and real parts and comparing with the similarly obtained phase of the reference signal. An example is given in Fig. 15 for a RTP plasma with double hydrogen-ice pellet injection, which leads to a doubling of the plasma density and a transient change in the poloidal field distribution.

The flexibility of the analysis method enables calculation of other quantities that may be of interest. One of these is the temporal variation in beat frequency (see Fig. 16), which is obtained by taking the derivative of the phase before comparison with the reference phase. Inherent to a mixing scheme, these IFs cannot be used to calculate the stability of an individual cavity. However, an algorithm check can be

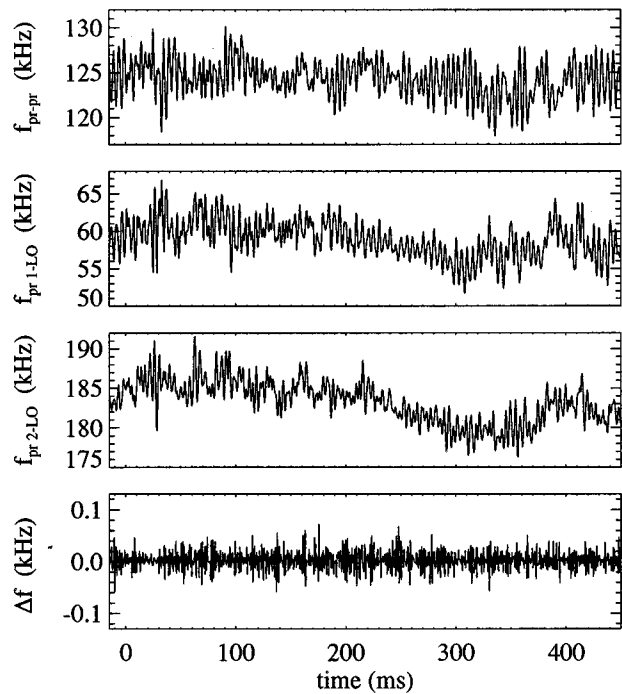


FIG. 16. Calculated beat frequency stability for the same discharge and channel as in Fig. 15. The first three plots directly give the instantaneous intermediate frequencies of each of the carriers. The total excursion agrees with the observed frequency bandwidth of Fig. 14. The 200 Hz modulation stems from the high-voltage power supply for the CO₂ laser. The fourth trace is the calculated sum of the three with sign chosen such that all laser frequencies cancel.

performed by calculating a sum of all three IFs, with the signs set such that a zero line should be obtained.

The analysis method can also be used to calculate the temporal evolution of the amplitude of each beat signal, by computing the modulus of the complex analytic signal. Figure 17 depicts the calculated amplitudes for the pellet-injected discharge. The antenna pattern of the corner cube mixers makes these devices rather sensitive to refraction. Therefore the signal amplitude varies throughout the discharge, and is severely decreased by the injection of the pellets. Since the amplitude of the detected signal is proportional to the product of the electric fields of the mixing waves, the probe-probe mix is influenced more severely than the probe-LO mixes.

V. EXPERIMENT

A. Refractive effects

In the RTP plasma the electron density under normal operating conditions does not exceed $1 \times 10^{20} \text{ m}^{-3}$. Even at these high densities, the line of sight for a beam with a wavelength of $432.5 \mu\text{m}$ deviates by less than 2 mm inside the plasma and may be approximated by a straight line. However, there will be a change in the angle with which the beam emerges from the plasma. This, in combination with the rela-

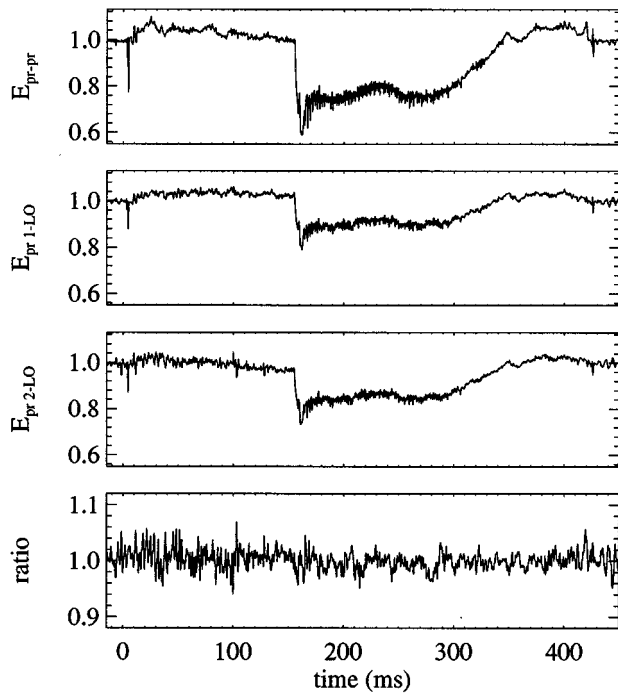


FIG. 17. Calculated signal amplitude for each of the frequency components for the same discharge and channel as in Fig. 15. Although only relatively small pellets are injected, the signal loss after pellet injection approaches 40% for this particular detector in the case of the probe-probe mix. The bottom plot shows the amplitude of the probe-probe mix, divided by the multiplied amplitudes of both probe-LO mixes. The ratio thus obtained is only dependent on the electric field amplitude of the LO laser, and hence refraction insensitive.

tively long distance between plasma and mixer array of 1.5 m, may nevertheless cause a significant displacement of the probing beam at the detector position of up to 2 cm. Since at RTP a continuous beam is used to probe the plasma, this displacement does not cause a complete loss of signal on certain detectors, as is the case with discrete chords. Nevertheless a decrease in signal level will occur, mainly because the change of incidence angle usually degrades the coupling to the detector, as demonstrated by Fig. 17.

Refraction causes the beams to be deflected away from the plasma center, and the line-integrated density and Faraday rotation profiles will be broadened. As a secondary effect, the length of the beam path will be increased. Since the refractive index in the plasma is below unity, the path length increase reduces the measured interferometric phase, and causes a narrowing of the line-integrated density profile, thus partly compensating the primary effect. The secondary effect does not affect the polarimetric phase measurement, however, since both probing beams experience the same path length increase.

In Fig. 18 the effect of refraction is shown for a medium- and a high-density discharge in RTP. An iterative Abel inversion technique is used to invert the path-length integrated measurements. Once an initial inversion (ignoring refraction effects) is obtained, a ray-trace code is used to determine the wave propagation through the plasma on the basis of the

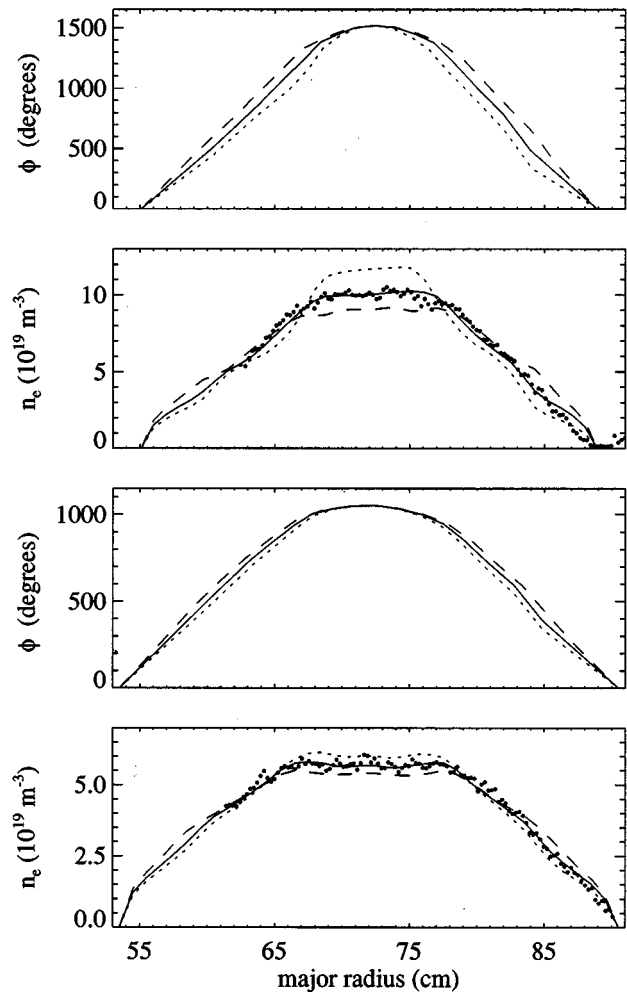


FIG. 18. Phase profiles, as well as the corresponding density profiles after inversion with the numerical inversion method of Yasutomo (Ref. 13). The inversion has been performed without correction for refraction (long dashes), with only a correction for the primary effect (short dashes), and with both effects corrected (solid line). The effects of the corrections on the phase profiles are also shown. The dots are from a multipoint Thomson scattering measurement, where the absolute signal level is scaled to the interferometer data because of lack of absolute calibration ($I_p=100$ (top) and 120 kA (bottom), $B_\phi=2.1$ T).

inverted density profile. For each detector, the position of the detected beam at the plasma midplane is then calculated, and this position is taken as an “apparent” detector position. Also the path length increase is calculated and compensated. A new inversion is then performed, using the apparent detector positions and the corrected phases. This procedure is repeated until the position shifts become negligible, normally after just two or three iterations. Figure 18 demonstrates that, in the case of high-density discharges, the neglect of refraction effect can introduce an error of up to 15% in the determination of the peak density.

B. Typical results

An illustrative measurement performed with the combined interferometer/polarimeter at RTP is shown in Fig. 19 in case of an electron-cyclotron (EC) heated discharge,

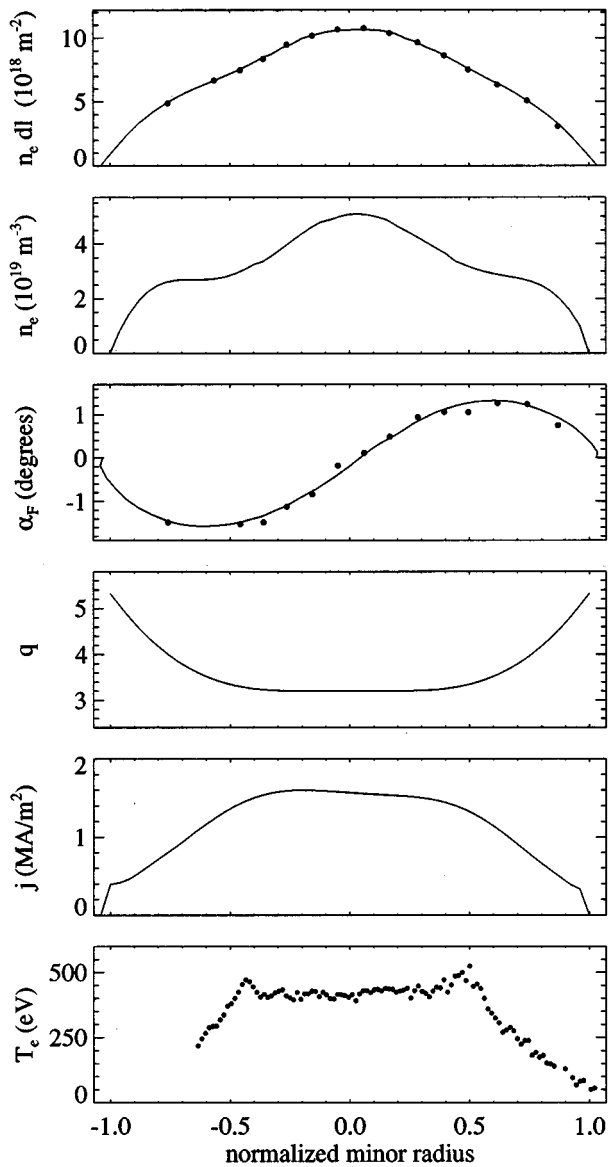


FIG. 19. Measured profiles of a 78.7 kA, 2.24 T discharge with 110 GHz heating at $r/a \approx +0.5$ (300 kW), approximately 90 ms after switch-on. Both the line-integrated and the inverted density profile are given, where inversion has been done with Parks method (Ref. 14). The third and fourth plots show a Faraday rotation profile, as well as the result of a restricted fit to the data points. Also plotted are the derived current density profile and the temperature profile, measured along a vertical chord with the multiposition Thomson scattering diagnostic at RTP. A clear flattening of both the temperature profile and the safety factor profile is observed.

where the EC power is deposited at approximately half the minor radius. As a result the temperature and, hence, the conductivity profile are deformed significantly, leading to a flat current density profile and a change in the corresponding

poloidal field distribution $B_{\text{pol}}(r)$. For the reconstruction, a natural safety factor profile was assumed.¹⁵ To account for a flattening and possibly a hollowing of the j -profile, a Gaussian was added to the q -profile [$q(r) \approx rB_{\text{tor}}/RB_{\text{pol}}$], the amplitude and width of which were fitted to match the data, using a χ^2 minimization criterion. The q -value at the edge was determined from the total amount of current in the discharge. The effects of refraction have been taken into account.

The time resolution of the measurements that are presented in Fig. 19 is typically several kHz and is fully determined by S/N considerations, since the basic (technical) limit imposed by the laser bandwidth allows frequency shifts up to several MHz. Realizing that the 19-channel interferometer/polarimeter system at RTP features also a fairly good spatial resolution of 14 mm per channel, one can conclude that with the introduction of the novel polarimeter scheme a new high-resolution diagnostic has become available for the purpose of plasma transport studies.

ACKNOWLEDGMENTS

The authors would like to acknowledge the support of the entire RTP team, in particular Frits Blik, Michiel Drabbe, Theo Oyevaar, and Allard van der Steege. This work was performed as part of the research program of the association agreement of Euratom and the "stichting voor Fundamenteel Onderzoek der Materie" (FOM) with financial support from the "Nederlandse organisatie voor Wetenschappelijk Onderzoek" (NWO) and Euratom.

- ¹J. H. Rommers and J. Howard, *Plasma Phys. Control Fusion* **38**, 1805 (1996).
- ²A. J. H. Donné and the RTP Team, *Plasma Phys. Rep.* **20**, 192 (1994).
- ³I. H. Hutchinson, *Principles of Plasma Diagnostics* (Cambridge University Press, Cambridge, 1987).
- ⁴P. Belland and J. P. Crenn, *Int. J. Infrared Millim. Waves* **10**, 1279 (1989).
- ⁵D. Véron, in *Infrared and Millimeter Waves, Vol. 2, Instrumentation* (1979), p. 67.
- ⁶H. R. Fettermann, P. E. Tannenwald, B. J. Clifton, C. D. Parker, and W. D. Fitzgerald, *Appl. Opt.* **33**, 151 (1978).
- ⁷E. V. Loewenstein, D. R. Smith, and R. L. Morgan, *Appl. Opt.* **12**, 398 (1973).
- ⁸M. Born and E. Wolf, *Principles of Optics* (Pergamon, Oxford, 1980).
- ⁹E. Hecht, *Optics* (Addison-Wesley, Reading, MA, 1987).
- ¹⁰N. Marcuvitz, *Waveguide Handbook*, M.I.T. Rad. Lab. Series, Vol. 10 (McGraw-Hill, New York, 1951).
- ¹¹A. V. Oppenheim and A. S. Willsky with I. T. Young, *Signals and Systems* (Prentice-Hall, London, 1983).
- ¹²J. Howard, *Infrared Phys.* **34**, 175 (1993).
- ¹³Y. Yasutomo, K. Miyata, S. Himeno, T. Enoto, and Y. Ozawa, *IEEE Trans. Plasma Sci.* **PS-9**, 18 (1981).
- ¹⁴H. K. Park, *Plasma Phys. Control Fusion* **31**, 2035 (1989).
- ¹⁵B. B. Kadomtsev, *Philos. Trans. R. Soc. London Ser. A* **322**, 125 (1987).